Highly-nonlinear hybrid silicon-plasmonic waveguides: analysis and optimization

Alexandros Pitilakis[1,*] and Emmanouil E. Kriezis[1]

[1] *Department of Electrical and Computer Engineering, Aristotle University of Thessaloniki, Thessaloniki GR-54125, Greece, Tel.: +30-2310-996362, Fax: +30-2310-996312*

We rigorously analyze nonlinear propagation in hybrid silicon-plasmonic (HSP) waveguides. Focusing on the relative importance of Kerr and free-carrier effects (FCE) originating from two-photon absorption, we establish a set of figures-of-merit applicable to any silicon-comprising waveguide. An optimized HSP design is proposed, deeply confining the optical-field in a nano-sized nonlinear-polymer gap formed between a metal-wedge and an underlying silicon-wire. An exceptionally high nonlinear parameter $\gamma > 10^4$ $\mathrm{m}^{-1}\mathrm{W}^{-1}$ is attained, combined with an FCE power-threshold larger than 1 W, even in CW. The formulation is also extended to multimode-waveguides, supported by two all-optical applications of an HSP nonlinear directional-coupler.

I. INTRODUCTION

The past decade's advances in nanofabrication and materials' science have unveiled numerous prospects for engineering compact and efficient optical devices with versatile functionality. Specifically, the nonlinear phenomena originating from the third-order $\chi^{(3)}$ susceptibility [1, 2], having outlasted every other contender towards all-optical signal-processing in integrated photonics, have re-emerged under more promising perspectives [3, 4]. Initial efforts focused on waveguide components built on the silicon-on-insulator (SOI) platform have established this technology as the de-facto for on-chip integration of photonics with electronics, but, at the same time, reached a fundamental barrier for nonlinear applications, due to the diffraction-limit. The latter upholds that classical index-contrast waveguides cannot be further reduced in size, thus halting photonic integrated circuits (PICs) miniaturization. Furthermore, as conventional SOI-waveguides cannot greatly benefit from novel highly-nonlinear materials, long interaction-lengths are typically required for any nonlinear application, which is identified as a bottleneck in footprint-reduction. Timely enough, the emergence of plasmonics [5] has provided unimagined opportunities with respect to integrated-component miniaturization and, consequently, potential for boosting nonlinear response. Surface-plasmon polariton (SPP) waves, localized on a metal-dielectric interface, can be confined in deeply subwavelength dimensions, way below the $\lambda/2$ diffraction-limit. The price paid is the increased propagation losses owing to the metal presence, that limits the effective length of SPP-waveguides. Exploiting features of both technologies, silicon-plasmonics [6, 7] is developing into a promising platform for integrated optics with viable potential for nonlinear applications.

The purpose of this is work is to identify a versatile waveguide platform for dense PICs, capable of rich nonlinear functionality accessed on micron-scale lengths. That said, probing the state-of-the-art waveguides built on the SOI platform, soon reveals two important points. Firstly, silicon waveguides' Kerr-effect magnitude is limited to a nonlinear parameter (γ) well below 10^3 $\mathrm{m}^{-1}\mathrm{W}^{-1}$. Secondly, they are plagued by two-photon absorption (TPA) in the near-infrared (NIR) [8]; what is more, the TPA-generated free-carriers effects (FCE) [4, 9] have a detrimental impact on nonlinear performance imposing upper limits on the maximum power and/or bitrate. For these reasons, millimeter-long waveguides and moderate average powers are typically required for the manifestation of any Kerr-type effect at the 10 Gbps benchmark bitrate [8]. In order to circumvent these limitations, we invest on an alternative SOI-compatible nonlinear waveguide platform. Hybrid silicon-plasmonic (HSP) waveguides [7, 10] fuse plasmonic and index-contrast guiding mechanisms by trapping light in a low-index gap between a metal and high-index dielectric, i.e. silicon. In this manner, they exhibit very high confinement that can result in a remarkably high nonlinear parameter, given a highly-nonlinear low-index gap dielectric. Furthermore, the TPA and FCE penalization is largely alleviated since light is not guided through the silicon-areas, similarly to the slot-waveguide designs [11]. This means that high powers can be safely launched allowing access to fully-developed Kerr-based phenomena in an effective-length scale of some tens of microns. The envisaged waveguide platform is SOI- and CMOS-compatible while it displays potential for further improvement in terms of γ, provided that novel materials with higher nonlinearity are successfully incorporated.

The paper is organized as follows. We first introduce a figure-of-merit (FoM) applicable to any nonlinear waveguide with losses. This basic FoM is a measure of the power needed for any Kerr-related nonlinear application, e.g., self-focusing, spectral broadening, cross-phase modulation, four-wave mixing, etc. We then extend the basic FoM to encompass silicon-comprising waveguides, by accounting for TPA and, particularly, FCE. All parameters are extracted from the waveguide eigenmode profile using a custom FEM-based solver and are derived from a rigorous vectorial nonlinear Schrodinger

* Corresponding author: alexpiti@auth.gr

equation (NLSE) formulation. Subsequently, we identify a promising family of HSP waveguides and propose an optimized design with respect to the established FoM. Extensive validation is provided, where the HSP are compared against standard SOI-based nonlinear-waveguides. Finally, the extension to multimode waveguides is outlined, corroborated by two example applications of an HSP nonlinear direction coupler (NLDC), namely, a power-dependent polarization-selective switch and an extinction-ratio booster for modulated signals.

II. FIGURES-OF-MERIT FOR NONLINEAR WAVEGUIDES

In this Section we establish a set of figures-of-merit for the comparison of nonlinear waveguides. Initially, conventional waveguides involving only standard Kerr-nonlinearity and linear losses are addressed. Subsequently, we move on to waveguides comprising silicon, where TPA and FCE come into play.

A. Conventional Nonlinear Waveguides

The Kerr-induced nonlinear phase-shift in a waveguide is given by $\Phi_{\text{Kerr}} = \gamma P_{\text{in}} L_{\text{eff}}$ [2], where γ ($\text{m}^{-1}\text{W}^{-1}$) is the nonlinear parameter derived from the $\chi^{(3)}$ susceptibility and the field-profile, P_{in} is the input peak-power and L_{eff} is the effective waveguide length accounting for all linear loss mechanisms. Assuming that nonlinear effects take place on the foremost part of a lossy waveguide, its length should typically not surpass the propagation length $L_{\text{prop}} = 1/\alpha$, where α (m^{-1}) is the linear-loss coefficient. In an L_{prop}-long waveguide, the linear insertion losses are 4.34 dB and the effective length is $L_{\text{eff}} = \int_0^{L_{\text{prop}}} e^{-\alpha z} dz = 0.6321 L_{\text{prop}}$. So, in order to characterize a lossy nonlinear waveguide in terms of its Kerr-efficiency we define a basic figure of merit (FoM)

$$\mathcal{F} = \gamma L_{\text{prop}} = \gamma/\alpha, \tag{1}$$

measured in W^{-1}. For example, consider the following waveguides: a typical SMF with 0.2 dB/Km losses and $\gamma = 1.4$ $\text{Km}^{-1}\text{W}^{-1}$ would have $\mathcal{F} = 30$ W^{-1} and a typical SOI waveguide with 1 dB/cm losses and $\gamma = 100$ $\text{m}^{-1}\text{W}^{-1}$ would have $\mathcal{F} = 4.3$ W^{-1}; in terms of this FoM, the fiber is a more efficient nonlinear waveguide, albeit on a orders-of-magnitude longer scale. Furthermore, it can be shown that the input peak-power needed for any Kerr-related nonlinear effect along an L_{prop}-long waveguide is inversely proportional to this FoM (since $\mathcal{F} \propto \Phi_{\text{Kerr}}/P_{\text{in}}$), i.e., waveguides with large $\mathcal{F}$ are more power-efficient. For instance, spectral FWHM-doubling of a guassian pulse [2] requires $P_{\text{in}} \approx 4/\mathcal{F}$, nonlinear switching in a directional coupler (due to desynchronization)[12] occurs at $P_{\text{in}} > 9/\mathcal{F}$, and a given degenerate four-wave-mixing (FWM) efficiency η [11] requires a CW pump power of $P_{\text{in}} \approx 3\eta^{1/2}/\mathcal{F}$.

B. Waveguides Comprising Silicon

Waveguides comprising silicon and operating at $\lambda < 2200$ nm exhibit TPA [8], a loss mechanism proportional to the optical power. Moreover, TPA is responsible for the generation of free-carriers which induce additional absorption and index-change [9] in the silicon-parts of the waveguide, which depend quadratically on the optical power. In view of these effects, the basic FoM introduced in the Section II A is in need of revising. For this purpose, we recast the vectorial single-channel NLSE [13] that fully describes the propagation of the slowly-varying envelope $A(z)$ of a CW signal in the following form

$$\frac{\partial A}{\partial z} = \left[i\Big(\gamma|A|^2 - f_D|A|^4\Big) - \frac{1}{2}\Big(\alpha + 2r\gamma|A|^2 + 2f_A|A|^4\Big) \right] A, \tag{2}$$

where A is measured in $\text{W}^{1/2}$ and moves at the $\exp(i\beta_0 z)$ phase-reference. In this equation, $\gamma = \text{Re}\{\gamma_c\}$ is the real-valued nonlinear parameter while $r = \text{Im}\{\gamma_c\}/\text{Re}\{\gamma_c\}$ represents the relative TPA-magnitude; γ_c is the complex-valued parameter fully characterizing the instantaneous electronic $\chi^{(3)}$-response of the waveguide [13]. The parameters f_A and f_D ($\text{m}^{-1}\text{W}^{-2}$) scale the free-carrier absorption (FCA) and dispersion (FCD). Note that Eq. (2) stands for a CW signal envelope, so all time-derivatives associated with dispersion and free-carrier temporal-dynamics disappear.

Before we give the expressions for these NLSE parameters, we will highlight the degradation of the basic figure-of-merit $\mathcal{F}$ upon the onset of TPA and FCE based on simple inspection of Eq. (2). Specifically, the FCD has an opposite sign to the Kerr nonlinearity thus reducing the nonlinear phase-shift, while both TPA and FCA contribute to an increase of the waveguide losses. Consequently, we can heuristically apply two power-dependent reduction terms to the $\mathcal{F}$ of Eq. (1), one that decreases the Kerr-nonlinearity ($\gamma' = \gamma - f_D|A|^2$) due to FCD and one that increases the losses ($\alpha' = \alpha + 2r\gamma|A|^2 + 2f_A|A|^4$) due to TPA and FCA:

$$\mathcal{F}' = \frac{\gamma'}{\alpha'} = \mathcal{F}\frac{1 - (f_D/\gamma)|A|^2}{1 + 2r\mathcal{F}|A|^2 + 2(f_A/\alpha)|A|^4}. \tag{3}$$

This expression is explicitly power-dependent and reduces to that of Eq. (1) for TPA-free waveguides. The parameters γ, α, $\mathcal{F}$, r, f_A and f_D depend only on the waveguide design (materials and geometry), whereas the power $|A|^2$ is dictated by the specific application targeted and resides in the order-of-magnitude of $1/\mathcal{F}$.

Focusing on the impact of free-carriers, the threshold power levels where FCE would severely degrade the Kerr-effect response can be easily discerned from Eq. (3). For instance, when $P_{\text{in}} > (\alpha/f_A)^{1/2}$ then FCA quenches the optical power thus hindering all nonlinear effects, and, when $P_{\text{in}} > \gamma/f_D$ then FCD dominates over the Kerr effect. In the latter case, the $\mathcal{F}'$ can even acquire large negative values, indicating a regime where FCD could

alternatively be used in the context of power-dependent refractive-index [14]; however, FCD is always accompanied by high FCA that limits its potential for this type of nonlinear applications.

C. Calculation of the Nonlinear Parameter

In order to calculate the complex-valued nonlinear parameter γ_c [13, 15] in nanophotonic waveguides, we employ a formulation that takes rigorously into account the cross-sectional distribution of the vector guided-modes, the material-heterogeneity and, finally, the anisotropy of the $\chi^{(3)}$ tensor properties for crystals like silicon,

$$\gamma_c = \frac{3\omega_0\varepsilon_0}{4\mathcal{N}^2}\sum_{\mu,\alpha,\beta,\gamma}^{x,y,z}\iint_{\infty}\chi^{(3)}_{\mu\alpha\beta\gamma}e^*_\mu e_\alpha e^*_\beta e_\gamma \mathrm{d}x\mathrm{d}y, \quad (4)$$

where $\mathcal{N} = \mathrm{Re}\{\iint(\mathbf{e}\times\mathbf{h}^*)\cdot\hat{\mathbf{z}}\mathrm{d}x\mathrm{d}y\}$, in Watt. In these expressions, $\mathbf{e}$ and $\mathbf{h}$ are the complex-valued, vectorial cross-section profiles of the electric and magnetic fields of the guided-mode and $\mathcal{N}$ is a normalization-integral associated with power-flow along the waveguide. The cross-section profile of the $\mu\alpha\beta\gamma$-component of the third-order susceptibility is given by

$$\chi^{(3)}_{\mu\alpha\beta\gamma} = \chi^{(3)}_{1111}\Bigg[\frac{\rho}{3}(\delta_{\mu\alpha}\delta_{\beta\gamma}+\delta_{\mu\beta}\delta_{\alpha\gamma}+\delta_{\mu\gamma}\delta_{\alpha\beta}) + (1-\rho)\sum_q R_{q\mu}R_{q\alpha}R_{q\beta}R_{q\gamma}\Bigg] \quad (5)$$

where ρ is the anisotropy factor in $\chi^{(3)}$ (≈ 1.27 for silicon [4], $\equiv 1$ for isotropic materials) and $R_{\mu\nu}$ are the elements of a 3×3 rotation matrix providing passage from the crystallographic coordinate system to the one used for the waveguide. In this work, we assume that silicon waveguides are fabricated along the $[\bar{1}\ \bar{1}\ 0]$ direction. The reference component $\chi^{(3)}_{1111}$, expressed in the crystallographic axes, is given by

$$\chi^{(3)}_{1111} = \frac{4}{3}\varepsilon_0 c n_0^2 n_2\Big(1+i\frac{\beta_{\mathrm{TPA}}}{2k_0 n_2}\Big), \quad (6)$$

where n_0 is the linear refractive index, n_2 (m^2/W) is the nonlinear index and β_{TPA} (m/W) is the TPA coefficient. Evidently, TPA can be seamlessly introduced as an imaginary part in n_2.

We stress that for absorbing waveguides the complex-valued normalization-integral $\mathcal{N}' = \iint(\mathbf{e}\times\mathbf{h})\cdot\hat{\mathbf{z}}\mathrm{d}x\mathrm{d}y$ [16], stemming from the most general form of the reciprocity theorem of Maxwell's equations, appears a more natural choice instead of $\mathcal{N}$. This latter choice, along with the generally complex-valued phase-constant, would necessitate for a more careful handling of the mode-orthogonality condition used in [13, 15]. Alternatively, one can include a small imaginary correction-term to $\mathcal{N}$, as introduced in [17]. However, for the full-range of waveguides considered in this work, we have numerically verified that all nonlinear-parameters show negligible differences when calculated following either the $\mathcal{N}$- or the $\mathcal{N}'$-based derivation. This is intuitively understood as, even in high-loss plasmonic waveguides, the imaginary part of the propagation constant (accounting for losses) is still roughly three orders-of-magnitude smaller compared to the real part, and thus acts in a perturbative way.

D. Free-Carrier Effects

Evolution of a single CW-signal according to Eq. (2), comprises the steady-state form of the free-carrier rate equation [4, 8] that complements the NLSE in the pulsed-regime. The rate equation monitors the temporal evolution of the effective free-carrier (electron-hole pair) density N generated via TPA along the waveguide

$$\frac{\partial N}{\partial t} = G - \frac{N}{\tau_{\mathrm{fc}}}, \quad (7)$$

where N is measured in m^{-3}, τ_{fc} is the effective carrier lifetime and G is the effective carrier generation rate that is proportional to the TPA-coefficient times the square of the optical-power. In the pulsed regime, G varies in both time and longitudinal distance, following the evolution of the complex field envelope, $A(z,t)$. In this case, Eq. (7) must be accounted for along the waveguide, together with the envelope's NLSE. For example, utilizing the split-step Fourier method (SSFM) [2], this can be easily accomplished by solving Eq. (7) in the frequency-domain according to

$$N(z,t) = \mathrm{IFT}\Big\{\frac{\mathrm{FT}\{G(z,t)\}}{\tau_{\mathrm{fc}}^{-1}-i\omega}\Big\}, \quad (8)$$

where FT/IFT is the Fourier-Transform pair at the envelope-frequency ω (in the vicinity of the carrier frequency ω_0). However, for CW signals, Eq. (8) reduces to the steady state solution $N(z) = G(z)\tau_{\mathrm{fc}}$ where the density varies only along the waveguide as the optical field is attenuated.

In the context of the NLSE, we aim at extracting parameters from the waveguide cross-section that quantify the various effects (attenuation, dispersion, nonlinearity, etc.) along the propagation of the optical field envelope. In this respect, it is instructive to qualitatively compare the HSP waveguides to the most representative SOI-based nonlinear waveguides in terms of FCE magnitude. We observe that, as opposed to the SOI-wire waveguide [Fig. 1(a)] the optical field of the slot and the HSP [Fig. 1(b) and (c), respectively] is almost exclusively outside the silicon areas. Taking into account that free-carriers are generated only in silicon and that their density is proportional to the square of the optical power, we can distinguish HSP waveguides from silicon-core ones in two ways [11]. Firstly, the rate of free-carrier

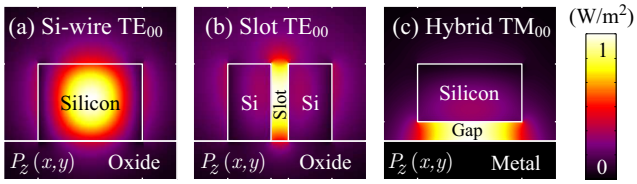

FIG. 1. Typical guided-power-density distribution, $P_z(x,y)$, for three waveguide types: (a) TE mode of a silicon-wire of $W \times H = 300 \times 200$ nm^2, (b) TE mode of a 50 nm-wide low-index slot formed between two $W \times H = 125 \times 200$ nm^2 Si-wires, (c) TM mode of a generic hybrid silicon-plasmonic waveguide formed by a 50 nm gap separating a metal-layer and a $W \times H = 300 \times 150$ nm^2 Si-wire. In all three waveguides, the cladding is a low-index dielectric with $n = 1.8$.

generation is comparatively smaller, reflected on smaller values of the relative TPA-parameter (r). Secondly, the free-carries are not co-localized with the maximum of the optical field (being confined inside the gap), so they are not as efficient in perturbing the field in an averaged sense; this aspect is contained partly in a confinement factor (referred to as Π in [13]) and partly in the effective carrier-lifetime, $\tau_{\rm fc}$. The former quantifies the fraction of optical intensity in the silicon-area of the waveguide assuming uniform free-carrier density therein, while the latter accounts for carrier diffusion, drifting, recombination and injection [4]. The value of $\tau_{\rm fc}$ depends on many factors including the silicon surface-to-volume ratio, the treatment at the material interfaces as well as any externally applied carrier-sweeping static-field [18]. Its calculation exceeding the scope of this work, we have adopted a fixed value of 1 nsec, typical for subwavelength SOI waveguides [4]. Instead, we focus on extracting a more rigorous expression for the carrier-field overlap factor, in place of the simple fractional confinement factor Π, in order to establish a better metric for FCE-penalization in silicon-comprising nonlinear waveguides. Nevertheless, $\tau_{\rm fc}$ is a crucial parameter for telecom applications since pulses shorter than $\tau_{\rm fc}$ suffer less from free-carrier effects; consequently, the metrics defined in Section II B can be considered pessimistic in terms of FCE-impairments, due to the CW illumination considered.

The cross-sectional distribution of the generated free-carrier density $N(x,y)$ is proportional to the TPA-induced rate-of-change of the optical-power density along the z-axis, $\partial P_{\rm TPA}/\partial z$ in W/m^3. In this work, we assume that the latter is proportional to $\beta_{\rm TPA}(x,y)$ times the square of the guided-power-density that is given by the axial component of the time-averaged Poynting-vector, $P_z(x,y) = {\rm Re}\{\frac{1}{2}(\mathbf{E} \times \mathbf{H}^*) \cdot \hat{\mathbf{z}}\}$, measured in W/m^2. Note that in a longitudinally invariant waveguide $P_z \gg (P_x^2 + P_y^2)^{1/2}$, meaning that it is safe to assume that P_z is the optical power density responsible for free-carrier generation; generally, one should use the total guided-power density, i.e. $|\mathbf{P}|$, since TPA is neither direction-selective nor bound to guided-modes only. The distribution of the free-carrier density (m^{-3}) is therefore

$$N(x,y,z) = \frac{\partial P_{\rm TPA}/\partial z}{2\hbar\omega_0}\,\tau_{\rm fc} = \frac{\beta_{\rm TPA}\tilde{P}_z^2|A|^4}{2\hbar\omega_0}\,\tau_{\rm fc}, \qquad (9)$$

where $\tilde{P}_z = P_z/\iint P_z {\rm d}x{\rm d}y$ is the normalized guided-power density (m^{-2}), i.e., $P_z = \tilde{P}_z|A|^2$, and $\hbar\omega_0$ is the energy of the absorbed photons. Now, in order to relate N to the induced change in refractive index ($\Delta n_{\rm fc}$) and absorption ($\Delta\alpha_{\rm fc}$) in silicon, we firstly assume that the density of photogenerated electrons and holes is approximately the same: $N_e = N_h = N$. Additionally, we adopt a Drude-model indicating a directly proportional relation of $\Delta n_{\rm fc}$ and $\Delta\alpha_{\rm fc}$ on N, where the respective scaling factors at $\lambda = 1550$ nm are $\sigma_n \approx 20 \times 10^{-28}$ m^3 and $\sigma_\alpha = 14.5 \times 10^{-22}$ m^2, respectively [9]. In this way, the complex-refractive-index perturbation profile within silicon, $\Delta u_{\rm fc} = [\Delta n_{\rm fc} + (i/2k_0)\Delta\alpha_{\rm fc}]$, is given by $\Delta u_{\rm fc} = \sigma_u\, N$ where $\sigma_u = [-\sigma_n + (i/2k_0)\sigma_\alpha]$. Note that in the commonly used Soref & Bennett experimental fittings for FCD [9], the electron and hole contribution to the index-change follow a $N_e^{1.05}$ and $N_h^{0.805}$ slope, respectively. However, the scope of this Section is to provide qualitative insight on the degradation due to FCE, so, for the sake of simplicity, we have adopted a linear Drude-fitting valid for relatively high free-carrier densities. In all our simulations, we insured that the average carrier-density is kept below 10^{26} m^{-3}.

Having calculated the cross-sectional distribution of the perturbations $\Delta n_{\rm fc}$ and $\Delta\alpha_{\rm fc}$, we can calculate the effective perturbation on the propagating optical field. Following the formulation of [13], we apply on $\Delta u_{\rm fc}$ the averaging

$$\langle \Delta u_{\rm fc} \rangle = \frac{\iint \Delta u_{\rm fc}(x,y,z)|\mathbf{e}|^2 {\rm d}x{\rm d}y}{\iint |\mathbf{e}|^2 {\rm d}x{\rm d}y} = \sigma_u \langle N \rangle, \qquad (10)$$

where the angled brackets denote the normalized overlap with the optical intensity $|\mathbf{e}(x,y)|^2$ in the infinite xy-plane; however, note that $\Delta u_{\rm fc}$ is non-zero only inside silicon where $\beta_{\rm TPA}(x,y)$ is non-zero. In a similar manner, the averaged carrier-density of Eq. (9) is

$$\langle N \rangle = \frac{\Xi}{2\hbar\omega_0}|A|^4\tau_{\rm fc}, \qquad (11)$$

where Ξ is a carrier-field overlap parameter given by

$$\Xi = \langle \beta_{\rm TPA}\tilde{P}_z^2 \rangle = \frac{\iint \beta_{\rm TPA}\tilde{P}_z^2|\mathbf{e}|^2 {\rm d}x{\rm d}y}{\iint |\mathbf{e}|^2 {\rm d}x{\rm d}y} \qquad (12)$$

and measured in m^{-3}W^{-1}. The parameter Ξ provides a spatial-measure of how the free-carriers perturb the optical field that incites them via TPA. For silicon-core waveguides, Ξ can be related to the dimensionless confinement factor Π [13] under the assumption of uniform field distribution exclusively inside the silicon area; in this case it holds that $\tilde{P}_z \approx A_{\rm Si}^{-1}$ and hence $\Xi \approx \beta_{\rm TPA}A_{\rm Si}^{-2}\Pi$, where $A_{\rm Si}$ is the silicon-area in the waveguide cross-section.

Returning to Eq. (2) and [13], the FCA and FCD perturbation terms that scale the FCE magnitude are given by

$$f_A|A|^4 = +\frac{\Gamma n_{\rm Si}}{n_{\rm eff}} \times \frac{1}{2}\langle \Delta\alpha_{\rm fc}\rangle, \tag{13a}$$

$$f_D|A|^4 = -\frac{\Gamma n_{\rm Si}}{n_{\rm eff}} \times k_0\langle \Delta n_{\rm fc}\rangle, \tag{13b}$$

respectively, where the minus-sign for the FCD term stems from our definition of f_D in Eq. (2), $n_{\rm Si}$ is the refractive index of silicon, $n_{\rm eff}$ is the effective index of the guided-mode and Γ is the dimensionless longitudinal-field enhancement factor (LEF)

$$\Gamma = c_0\varepsilon_0 n_{\rm eff}\mathcal{N}^{-1} \iint_{\infty} |\mathbf{e}|^2 {\rm d}x{\rm d}y. \tag{14}$$

The LEF is equal to unity for purely TEM, TE and TM modes, while $\Gamma > 1$ for hybrid-modes. For nanophotonic Si-waveguides, the factor $\Gamma n_{\rm Si}/n_{\rm eff}$ contributes to approximately a two-fold increase in the FCE magnitude, Eqs. (13), with respect to large cross-section SOI-waveguides where $\Gamma \approx 1$ and $n_{\rm eff} \approx n_{\rm Si}$. The final expressions for the parameters f_A and f_D are the following

$$f_A = \frac{\Gamma n_{\rm Si}}{n_{\rm eff}} \times \frac{\Xi\tau_{\rm fc}}{2\hbar\omega_0} \times \frac{1}{2}\sigma_\alpha, \tag{15a}$$

$$f_D = \frac{\Gamma n_{\rm Si}}{n_{\rm eff}} \times \frac{\Xi\tau_{\rm fc}}{2\hbar\omega_0} \times k_0\sigma_n. \tag{15b}$$

Note that these FCE parameters are implicitly related to the absolute TPA-rate, $\mathrm{Im}\{\gamma_c\} = r\gamma$, since $\Xi \approx 2r\gamma/A_{\rm Si}$. This expression holds for large cross-section silicon-core waveguides, while it only qualitatively hints at how the FCE parameters scale in HSP waveguides. In view of the latter, the carrier-field overlap parameter Ξ constitutes a rigorously generalized metric for any silicon-comprising waveguide.

E. Waveguide Optimization Outlines

Concerning the relative importance of the Kerr-effect vs. the FCE, a secondary FoM can be defined

$$\zeta_{\rm fc} = \frac{\gamma\, n_{\rm eff}}{\Xi\,\Gamma}, \tag{16}$$

measured in m^2. This FoM is derived as follows: according to Eq. (3), the threshold input CW power where FCD overwhelms the Kerr-effect can be approximated by $P_{\rm th,FCD} = \gamma/f_D = \zeta_{\rm fc}\,\varpi$, where $\varpi = 2\hbar c_0/(\tau_{\rm fc} n_{\rm Si}\sigma_n)$ is approximately 9.2×10^9 W/m^2 using the parameter values adopted in this work; a similar expression can be formulated for the threshold power related to FCA. In order to make full use of the Kerr-effect, a waveguide with a relatively high FCE-threshold would be required. More specifically, for FCD-free performance near the critical power-level for Kerr-applications ($\approx 1/\mathcal{F}$), a waveguide should ideally satisfy $P_{\rm th,FCD} \gg 1/\mathcal{F}$ or, equivalently, $\mathcal{F}\zeta_{\rm fc}\varpi \gg 1$.

From the viewpoint of silicon-based waveguide (conventional or hybrid) optimization for Kerr-type nonlinear applications, we can conclude that a maximum $\mathcal{F}$ and $\zeta_{\rm fc}$ is sought. Alternatively, when the operating-power is apriori set, then the $\mathcal{F}'$ of Eq. (3) can be used as a single overall FoM.

III. HYBRID SILICON-PLASMONIC WAVEGUIDES

A waveguide platform for integrated photonic components aimed at $\chi^{(3)}$-nonlinear applications should combine acceptable losses with strong mode-confinement localized in a highly nonlinear material. Additionally, efficient interfacing with conventional waveguides integrated in a common hybrid-motherboard is desired. The above specifications can be satisfied by what is collectively referred to as Hybrid Silicon-Plasmonic (HSP) waveguides [10].

A. Waveguide geometry and supported modes

Figure 2 depicts three possible HSP waveguide designs that have already been proposed in [7], [19] and [20], respectively, albeit in a context different from nonlinear optics. Their common feature is a silicon region separated from a metal-film by a low-index gap material. When the latter is actually a highly-nonlinear material, then, the HSP waveguide's nonlinear parameter (γ) can be considerably boosted by means of increased mode-confinement. In the design of Fig. 2(a), referred to as the standard conductor-gap-silicon (CGS) waveguide, both low-index-dielectric and metal regions have the same width as the silicon area whereas in the design of Fig. 2(b) they are allowed to an infinite extent. In the latter design, referred to as "extended" CGS, an extra parameter is invoked, namely, an inverted metal rib that aids in further localizing the electric field. We could also invoke a thin slab next to the silicon-wire (thus changing the structure to a silicon-rib) that would provide additional electric contacts for sweeping the TPA-generated free-carriers and thus reducing their effective lifetime ($\tau_{\rm fc}$). This silicon-slab is omitted in all subsequent calculations, since it marginally affects optical waveguiding and is relevant primarily to the rigorous calculation of $\tau_{\rm fc}$, not undertaken in this work. Finally, the design of Fig. 2(c) replaces the inverted metal rib with an inverted wedge, a feature leading to more pronounced plasmonic-confinement. In what follows, we focus on the extended CGS designs of Fig. 2(b) and (c) for which a fabrication procedure has been recently outlined [19].

For a sufficiently small gap between silicon and metal, the fundamental TM-like (y-polarized) mode supported

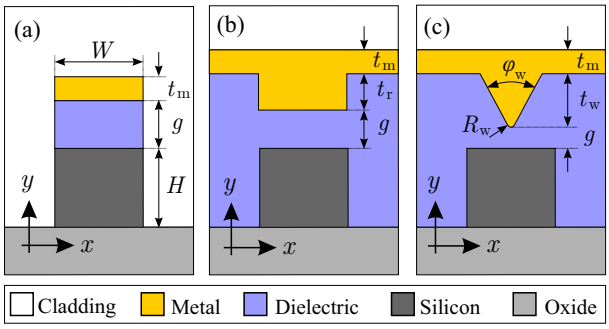

FIG. 2. Cross-section of the hybrid silicon-plasmonic (HSP) waveguides: (a) standard CGS (b) extended CGS with inverted metal-rib (c) extended CGS with inverted metal-wedge.

by the HSP waveguides is accommodated almost exclusively inside the nonlinear material, therefore leading to an exceedingly high γ as the gap area is reduced. However, reducing the gap also increases the Ohmic loss since the field penetrates relatively more into the metal; consequently, the propagation losses (apart from obvious technological constraints) will set lower bounds on the dimensions of the gap. On the contrary, when the gap thickness is increased, the TM-like mode degenerates to a typical SOI photonic mode, provided that the silicon-area is sufficiently large. In a similar manner, efficient interfacing between the HSP and conventional SOI waveguide is possible [7] by simply removing the metal. Finally, if the underlying silicon ridge is wide enough, the HSP waveguide additionally supports a TE-like photonic mode; this mode's losses are smaller than those of the TM, but in any case non-negligible, especially for small gaps. In this Section, we opted for silicon wires larger in the vertical dimension so as to favor the TM-mode (over the TE) of the underlying SOI waveguide, which could serve as feed to the HSP waveguide, all integrated in a common wafer.

B. Material choices

The HSP waveguides are targeted for applications in the telecom C-band, so $\lambda = 1550$ nm throughout. In order to minimize Ohmic losses, we selected silver (Ag), characterized by a refractive index of $n_{\rm Ag} = 0.145 + i11.4$ [21]. For the gap material, the highly-nonlinear organic polymer DDMEBT is selected [22], described by a linear and nonlinear index of $n_0 = 1.8$ and $n_2 = 1.7 \times 10^{-17}$ m^2/W, respectively. Although materials with an order-of-magnitude higher nonlinear index have been reported, e.g., the polydiacetylene para-toluene sulfonate (PDA/pTS) [23] or the polystyrene [24], they have not yet been demonstrated in planar subwavelength photonic structures. Other nonlinear material candidates are chalcogenide glasses [25], possessing a n_2 equivalent to that of the DDMEBT; unfortunately, their higher linear indices ($n_0 \approx 2.4$) disfavor both confinement and propagation losses. Furthermore, we stress that DDMEBT is free from TPA, and thus also from FCE. The linear and nonlinear indices of silicon are $n_0 = 3.45$ and $n_2 = 2.5 \times 10^{-18}$ m^2/W [13], respectively, and for silicon-dioxide $n_0 = 1.45$ and $n_2 = 2.7 \times 10^{-20}$ m^2/W, respectively. The TPA parameter of silicon is $\beta_{\rm TPA} = 5 \times 10^{-12}$ m/W [13]. The cladding here considered is air, but, in any case, this material negligibly affects the optical waveguiding in the designs of Fig. 2(b) and (c).

The non-local ponderomotive force resulting in a Kerr-like $\chi^{(3)}$-response from the metal [26] was found to have a negligible effect on γ, since the electric-field does not penetrate deeply inside the metal. Finally, the maximum electric-field intensity was checked to be below the typical dielectric strength of thin polymers layers to avoid breakdown.

C. Optimization of HSP waveguides

We employ an in-house finite-element method (FEM) spectral mode-solver [27] to extract the eigenmodes of a given waveguide geometry and operating wavelength. The FEM modeling allows for arbitrarily heterogeneous geometries, with respect to both the linear and the nonlinear properties of the materials involved. The waveguide cross-section is discretized with triangular finite elements, each one attributed the set of material parameters introduced in Sections II C, II D and III B $(n_0, n_2, \beta_{\rm TPA}, \rho, \sigma_u)$. The linear index is the only one actually intervening in the eigenmode solver, while the rest are subsequently used for the calculation of the NLSE-parameters from the extracted linear eigenmode profile. In every HSP waveguide, the parameter that has the greatest effect on the nonlinear response is the gap size, so, we initially focus on a simplified version of the extended CGS design of Fig. 2(b). We set $W \times H = 220 \times 340$ nm^2 corresponding to a subwavelength SOI-wire supporting a well-formed TM-like mode, we momentarily ignore the inverted metal rib ($t_r = 0$), and we set the silver-film thickness to $t_m = 50$ nm. Subsequently, we calculate all the critical nonlinear parameters as a function of the gap-size (g), ranging from 300 nm down to 5 nm. Figure 3(a) depicts the fundamental tradeoff between plasmonic confinement and Ohmic losses, reflected on the opposite trend between the nonlinear parameter γ and the propagation length $L_{\rm prop}$. When the gap is large, the mode of the HSP waveguide degenerates to that of a standard Si-wire leading to a $\gamma \approx 100$ m^{-1}W^{-1} and an increasing $L_{\rm prop}$, eventually limited only by the fabrication-quality, e.g. 1 dB/cm. On the contrary, as the gap decreases, the TM-mode shifts to the highly-confined and thus lossy HSP regime, where the increase in γ is inversely proportional to the decrease in the effective mode-area ($A_{\rm eff}$). Figure 3(b) depicts the effect of the gap on the TPA-ratio $r = {\rm Im}\{\gamma_c\}/{\rm Re}\{\gamma_c\}$ and the carrier-field overlap factor Ξ, Eq. (12); the former decreases with the gap-decrease since the HSP mode resides

mostly outside silicon, while the latter decreases slowly but rises sharply below the threshold gap of 20 nm. This threshold gap is due to the less-efficient confinement from the side of the silicon/dielectric interface (as compared to the dielectric/metal one), and can be pushed lower in narrower Si-wires (smaller W). Finally, in Fig. 3(c), we witness the plasmonic enhancement as the gap decreases, resulting in an increase in both $n_{\rm eff}$ and the factor Γ (LEF), Eq. (14).

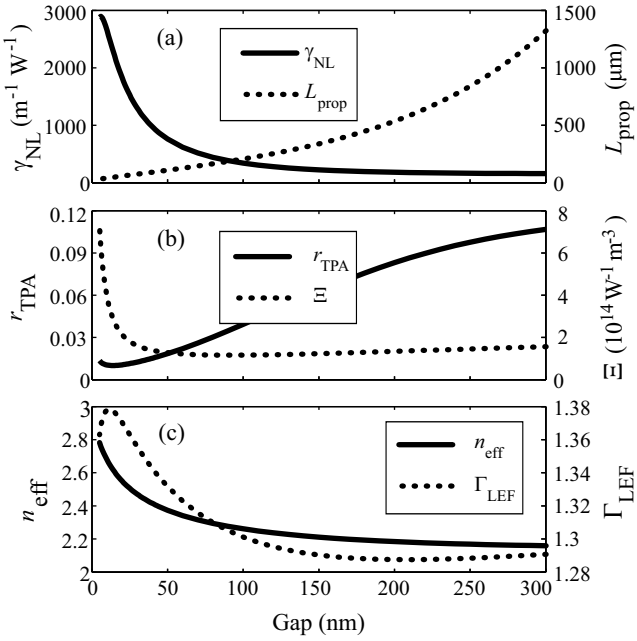

FIG. 3. Effect of gap size in the extended CGS waveguide with $W \times H = 220 \times 340$ nm^2, $t_{\rm m} = 50$ nm and $t_{\rm r} = 0$. (a) Nonlinear parameter and propagation length, (b) TPA-ratio and carrier-field overlap factor, (c) effective-index and longitudinal-enhancement factor.

Figure 4 depicts the effect of the gap on the aggregate FoM parameters $\mathcal{F}$ and $\zeta_{\rm fc}$, defined in Section II. Large gaps lead to a high $\mathcal{F} > 0.2$ W^{-1}, but also to a low $\zeta_{\rm fc} \approx 10^{-12}$ m^2, indicating a low FCD power-threshold of 10 mW (CW). On the contrary, for a gap of 10-20 nm, $\mathcal{F}$ and $\zeta_{\rm fc}$ peak at about 0.1 W^{-1} and 15×10^{-12} m^2, respectively. In this case the FCD power threshold is increased to 150 mW but, still, the critical power-level for Kerr-effect applications ($\propto \mathcal{F}^{-1}$) is a hundred times higher. A small increase in the FoM of this HSP waveguide design [Fig. 3(b)] is possible by optimization of all its geometrical parameters leading to $\mathcal{F} = 0.15$ W^{-1} and $\zeta_{\rm fc} = 40 \times 10^{-12}$ m^2; these values are obtained by setting $g = 20$ nm, $H = 220$ nm, $t_{\rm m} = 50$ nm and the optimum $W = 140$ nm and $t_{\rm r} = 70$ nm [28].

We now focus on an alternative cross-sectional patterning of the metal-film which can offer enhanced plasmonic confinement, thus improving the FoM of the HSP waveguide. A waveguide consisting of a laterally infinite metal-wedge in a homogeneous cladding supports a plasmonic mode localized at the tip of the wedge [29]. In

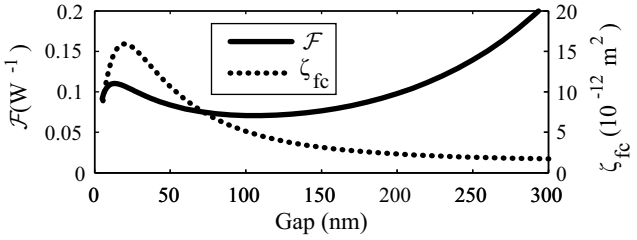

FIG. 4. Effect of gap size on figures-of-merit $\mathcal{F}$ and $\zeta_{\rm fc}$, for the extended CGS waveguide with $W \times H = 220 \times 340$ nm^2, $t_{\rm m} = 50$ nm and $t_{\rm r} = 0$.

the presently addressed nonlinear-waveguide context and for our material choices (a silver wedge in a DDMEBT cladding), the propagation length and nonlinear parameter are $L_{\rm prop} \approx 50$ μm and $\gamma \approx 10^3$ m^{-1}W^{-1}, respectively, leading to a $\mathcal{F}$ of 0.05 W^{-1}. However, bringing the metal-wedge tip in close proximity to a laterally aligned underlying SOI waveguide, increases the confinement and consequently the nonlinearity, thanks to the hybrid guiding mechanism. To this end, we investigate the effect of the structural parameters of this HSP waveguide, Fig. 2(c), on $\mathcal{F}$ and $\zeta_{\rm fc}$; the parameters of the inverted wedge are the tip-curvature radius ($R_{\rm w}$), the angle ($\varphi_{\rm w}$) and the height ($t_{\rm w}$). In our modeling, the width of the base of the triangular wedge is implicitly dependent on the rest of its parameters ($R_{\rm w}$, $\varphi_{\rm w}$ and $t_{\rm w}$). The investigation with respect to the three wedge-parameters is presented in Fig. 5. In all cases, the Si-wire is $W \times H = 220 \times 220$ nm^2, the silver film is $t_{\rm m} = 50$ nm and the gap is $g = 20$ nm. When not parametrically varied, the wedge parameters are fixed at $R_{\rm w} = 1$ nm, $\varphi_{\rm w} = 2\tan^{-1}(0.5) = 53.2°$ and $t_{\rm w} = 100$ nm. As depicted in Fig. 5, both $\mathcal{F}$ and $\zeta_{\rm fc}$ increase with decreasing $R_{\rm w}$ and $\varphi_{\rm w}$, while the scale of the wedge (expressed in terms of its vertical height $t_{\rm w}$) does not have an important impact. To visualize the influence of $\varphi_{\rm w}$ and $R_{\rm w}$, we plot the cross-sectional distribution of the normalized electric-field intensity of the TM$_{00}$ mode, for three wedge-parameter configurations. Specifically, Fig. 6(a), (b) and (c) correspond to the reference design, to a larger wedge-angle and to a larger curvature-radius, respectively; evidently, increasing $\varphi_{\rm w}$ or $R_{\rm w}$ leads to reduced confinement. Furthermore, we ascertained that the FoM do not drop appreciably neither for $W > 220$ nm (optimal Si-width) nor for reasonable horizontal misalignments between the wedge and the underlying Si-wire. This constitutes an attractive feature since the waveguide design is relatively insensitive to fabrication-imperfections concerning lateral-resolution accuracy.

IV. COMPARATIVE ASSESSMENT AND VALIDATION

In this Section we firstly compare the most promising silicon-comprising waveguides for nonlinear applications

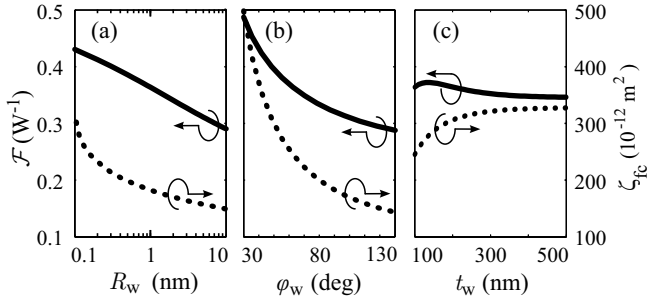

FIG. 5. Parametric investigation of the inverted metal-wedge HSP waveguide with respect to (a) the wedge-tip curvature-radius R_w, (b) the wedge-angle φ_w and (c) the wedge-thickness t_w. In all cases: $W \times H = 220 \times 220$ nm^2, $t_m = 50$ nm and $g = 20$ nm. When not parametrically varied: $R_w = 1$ nm, $\varphi_w = 2\tan^{-1}(0.5) \approx 53.2°$ and $t_w = 100$ nm.

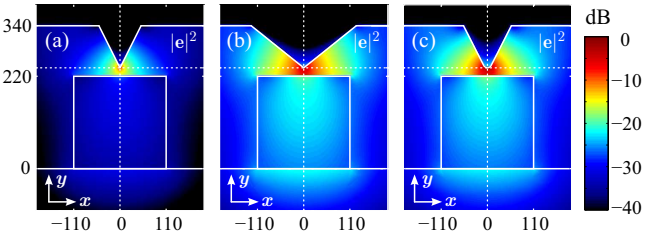

FIG. 6. Normalized intensity distribution of the inverted metal-wedge HSP waveguide TM_{00} mode. (a) Reference design with $R_w = 1$ nm and $\varphi_w = 53.2°$, (b) larger wedge-angle $\varphi_w = 102.7°$, (c) larger tip-curvature $R_w = 10$ nm. In all cases: $W \times H = 220 \times 220$ nm^2, $t_m = 50$ nm and $g = 20$ nm.

and subsequently call upon the nonlinear Schrödinger equation (NLSE) in order to validate the salient points of the conducted investigation. Our main target is to establish the relation between the proposed FoM and practically meaningful quantities, namely, the nonlinear-threshold (NLT) powers where the FCE performance-penalties become important.

A. Comparative Assessment

As discussed in Section II E, in order to assess the comparative performance of silicon-comprising nonlinear waveguides in terms of the Kerr-effect, we need to maximize both $\mathcal{F}$ and ζ_{fc}, given by Eqs. (1) and (16), respectively. Additionally, it was discussed that $\mathcal{F}\zeta_{fc}\varpi \gg 1$ is desired for negligible FCD-impairment in the CW-regime.

Up to date, the most promising silicon-based nonlinear waveguides are the standard SOI-wire/rib [30] and the nonlinear-slot [11]. Even though SOI-wire/rib are the most technologically mature, their high $\mathcal{F} > 1$ W^{-1} is only available in the 1 cm length-scale, while their low FCD-threshold limits their overall potential for Kerr-applications ($\mathcal{F}\zeta_{fc}\varpi \approx 0.05$). Compared to SOI-wire/rib, the nonlinear-slot designs can offer a slightly smaller $\mathcal{F}$, in the order of 0.5 W^{-1}, along with an order-of-magnitude improvement to the length-scale ($L_{prop} >$ 1 mm) and to the FCD-threshold ($\mathcal{F}\zeta_{fc}\varpi \approx 0.5$). In a similar manner, the optimized HSP waveguide with the inverted metal-wedge, can provide equivalent FoM to the nonlinear-slot (accommodating the same nonlinear polymer) but on a length-scale twenty times smaller, leading to even more compact devices. Moreover, the inverted metal-wedge HSP waveguide penetrates the FCD-free range of $\mathcal{F}\zeta_{fc}\varpi > 1$ as the gap is reduced below 10 nm. On the contrary, $\mathcal{F}\zeta_{fc}\varpi$ peaks at 0.02 for the extended CGS (for $g = 15$ nm in Fig. 4) and at 0.7 for the nonlinear-slot design [11] (for a slot-width of 50 nm). It should be noted that in the latter design we assumed 1.6 dB/cm losses and calculated the parameters γ and ζ_{fc} based on our formulation. Other silicon-plasmonic waveguides already proposed [21, 31] are less promising compared to this HSP design, due to low $\mathcal{F}$ and/or ζ_{fc}.

Finally, we stress that in both SOI-wire/rib and nonlinear-slot designs the propagation-length is delimited by the scattering losses related to fabrication-imperfections of the waveguide sidewalls; conversely, the losses of HSP design are dominated by Ohmic-losses owing to the metal presence, so, fabrication-imperfections are less likely to further increase the losses. The comparative advantage of HSP waveguides over nonlinear-slot ones, is the potential for considerably larger nonlinearity (owing to the plasmonic confinement) that compensates for the high plasmonic losses while keeping the required interaction lengths below the 0.1 mm regime. As a concluding remark, the metal-wedge was chosen as a paragon of extreme plasmonic-confinement and was thus incorporated in optimizing HSP waveguides; actually, any nano-sized feature (such as simply patterning the metal-layer into a narrow stripe), when methodically optimized, can potentially lead to equivalent performance.

B. Validation by NLSE

In this Section, the NLSE is employed to model the CW single-mode nonlinear propagation in order to quantify the penalties arising from TPA and FCE. As comparison metrics, we use the nonlinear phase-shift ($\Delta\Phi_{NL}$) and the nonlinear insertion-losses (IL_{NL}). These quantities evolve along the waveguide and their output-values can be easily calculated by numerical integration of the NLSE, Eq. (2), for a given input power (P_{in}) and waveguide length (L). The NLSE parameters (namely α, γ, r, f_A and f_D) are derived from the waveguide cross-section using our FEM-based eigenmode solver.

The nonlinear phase-shift $\Delta\Phi_{NL}$ is the phase-difference from the reference linear phase-accumulation ($\beta_0 L$) and can be easily extracted from the angle of the slowly-varying signal-envelope, i.e. $\Delta\Phi_{NL} = -i\ln(A/|A|)$. This phase-shift has contributions from the Kerr-effect and the linear-losses, as well as from the rest of the nonlinear-effects, i.e., $\Delta\Phi_{NL} = \Phi_{Kerr} + \Phi_{non\text{-}Kerr}$. In our approach,

$\Phi_{\text{Kerr}} = \gamma P_{\text{in}} L_{\text{eff}}$ (when TPA and FCE are switched off) is positive-valued and beneficial while $\Phi_{\text{non-Kerr}}$ is negative-valued and associated with TPA and FCE impairments. The absolute value of $\Phi_{\text{non-Kerr}}$ increases according to two power-dependent mechanisms. Firstly, as the nonlinear losses (TPA and FCA) reduce the L_{eff} from its value in the linear-regime, which is equivalently perceived as a contribution in $\Phi_{\text{non-Kerr}}$, and, secondly, as the FCD induces an index-change of opposite-sign to the Kerr effect. Consequently, in order to quantify the NLT-power where the non-Kerr contribution dominates the $\Delta\Phi_{\text{NL}}$, we define the ratio

$$r_\delta = \frac{-\Phi_{\text{non-Kerr}}}{\Phi_{\text{Kerr}}} = \frac{\gamma P_{\text{in}} L_{\text{eff}} - \Delta\Phi_{\text{NL}}}{\gamma P_{\text{in}} L_{\text{eff}}} \geq 0. \qquad (17)$$

that rises from zero as the the power is increased. The NLT for the phase-degradation due to TPA and FCE can be associated with the power P_{in} where $r_\delta > 1$.

The nonlinear insertion-losses IL_{NL} account only for the TPA- and FCA-induced attenuation, and are given by the overall attenuation extracted from the amplitude of the signal-envelope in the NLSE, Eq. (2), if we exclude the linear-losses

$$\text{IL}_{\text{NL}} = \frac{|A|^2}{P_{\text{in}}} \exp(L/L_{\text{prop}}). \qquad (18)$$

Figure 7 depicts the metrics r_δ and IL_{NL} as a function of the input optical power for three nonlinear waveguides, namely a SOI-wire [13], a nonlinear-slot [11] and our optimized inverted metal-wedge HSP design; the corresponding NLSE parameters are given in Table I. For the purpose of comparison, the waveguide-length is set to $L = L_{\text{prop}}$ for each of the three designs. The vertical dotted lines in Figs. 7(a) and (b) correspond to the NLT-powers $P_{\text{th,FCA}} = (\alpha/f_A)^{1/2}$ and $P_{\text{th,FCD}} = \gamma/f_D$, and can be associated with amplitude- and phase-penalization due to FCA and FCD, respectively. It is readily inferred that these NLT-powers correspond to $\text{IL}_{\text{NL}} \approx -2.5$ dB and $r_\delta \approx 0.7$, respectively, values that are representative measures of the FCE-induced penalties on the propagation of CW-signals along L_{prop}-long waveguides. Additionally, the HSP outperforms both nonlinear-slot and SOI-wire waveguides in terms of FCE-penalization, successfully withstanding CW-powers above 1 W. Finally, we note that r_δ can exhibit a peak, indicating an optimal power-regime for using the FCD as a phase-manipulating nonlinear effect; this feature is especially pronounced in the SOI-waveguide, e.g. at $P_{\text{in}} = -6$ dBW in Fig. 7(b).

Concerning the pulsed-regime, it is important to stress that the corresponding NLT-powers are considerably increased with respect to the CW-regime ones. This is generally true for pulses shorter than the carrier-lifetime ($\tau_{\text{fc}} = 1$ ns) and for low repetition-rates [4]. In these scenarios, even though the FCE are triggered instantaneously due to TPA, they do not considerably affect the pulse that generates them because the accumulation-time for the build-up of a critical carrier-density exceeds the pulse-duration. Consequently, both FCD and FCA

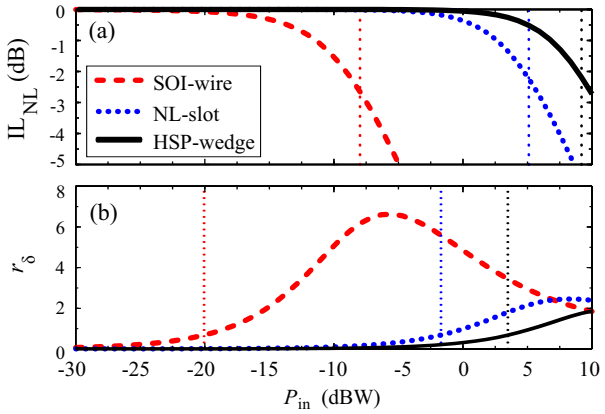

FIG. 7. NLSE-calculated (a) nonlinear insertion-losses IL_{NL} and (b) Nonlinear phase-shift fraction r_δ as a function of input-power. The dotted lines in each subfigure correspond to the threshold powers $P_{\text{th,FCA}} = (\alpha/f_A)^{1/2}$ and $P_{\text{th,FCD}} = \gamma/f_D$, respectively, for each waveguide. The waveguide parameters are given in Table I.

TABLE I. Nonlinear waveguide NLSE parameters.

NLSE-parameter	SOI-wire[a]	NL-slot[b]	HSP-wedge[c]
γ ($\text{m}^{-1}\text{W}^{-1}$)	117	286	12400
r_{TPA} (%)	19	0.69	0.072
L_{prop} (μm)	43430	2710	29.3
f_D ($\text{m}^{-1}\text{W}^{-2}$)	13118	358	5546
f_A ($\text{m}^{-1}\text{W}^{-2}$)	1173	32	496

[a] TE-mode, Si-wire is 400×340 nm^2, 1 dB/cm losses, DDMEBT cladding, $\tau_{\text{fc}} = 1$ ns.
[b] TE-mode, DDMEBT-slot is 140 nm-wide and formed by two 200×220 nm^2 Si-wires, 1.6 dB/mm losses [11], $\tau_{\text{fc}} = 1$ ns.
[c] TM-mode, DDMEBT-gap is 20 nm, Si-wire is 200×220 nm^2, Ag-wedge is $t_w = 100$ nm, $\varphi_w = 53.2°$ and $R_w = 1$ nm [Fig. 2(c)], $\tau_{\text{fc}} = 1$ ns.

power-thresholds are at least 10–20 dB higher than the CW-ones. This allows for higher peak-powers and, consequently, more pronounced Kerr-response than anticipated from the CW-regime, particularly for the worst-performing SOI-waveguides [30]. Even for NRZ systems (where long sequences of "1" bits are anticipated to suffer more) and/or high repetition-rates (where the free-carriers generated by one pulse can considerably affect the following ones), the FCE power-thresholds are still higher than those calculated for CW-radiation. In overall, the estimates of this Section mainly provide relative-figures for the NLT-powers over which FCE become important in different waveguide designs. Nevertheless, they can be employed in the context of comparative waveguide assessment and optimization, since the penalization always scales with the factor ζ_{fc}, in the pulsed, as well as in the CW-regime.

V. MULTIMODE WAVEGUIDE EXTENSION

In this Section we extend our formulation in order to include the nonlinear mode-coupling in multimode silicon-comprising waveguides. In this case, instead of a single equation, we presently have a set of K coupled NLSE, where each one describes the spatiotemporal evolution of the kth-mode's complex-valued slowly-varying envelope, $A_k(z,t)$. Following the notation of [13], the envelope of the kth-mode evolves as

$$\frac{\partial A_k}{\partial z} = \left[\sum_{n=1}^{\infty} i^{n+1}\frac{\beta_n^{(k)}}{n!}\frac{\partial^n}{\partial t^n}\right]A_k - \frac{\alpha_k}{2}A_k + T_{3\mathrm{o}}^k + T_{\mathrm{fc}}^k. \quad (19)$$

Apart from the self-acting nonlinear-effects described in Section II, nonlinear coupling between the modes additionally arises from the third-order susceptibility term ($T_{3\mathrm{o}}^k$) as well as due to TPA-generated free-carriers term (T_{fc}^k), where

$$T_{3\mathrm{o}}^k(z,t) = \sum_{l,m,n=1}^{K} i\gamma_{klmn}A_l A_m^* A_n \exp(i\Delta\beta_{klmn}z), \quad (20)$$

$$T_{\mathrm{fc}}^k(z,t) = \sum_{l=1}^{K} i\delta_{kl}A_l \exp\left\{i[\beta_0^{(l)} - \beta_0^{(m)}]z\right\}, \quad (21)$$

In these expressions, γ_{klmn} (a constant) is the generalization of the nonlinear parameter γ_c of Eq. (4) and describes how the kth-mode is affected by the lmn-modes through the instantaneous $\chi^{(3)}$-processes, i.e. the Kerr and TPA effects. Additionally, $\delta_{kl}(z,t)$ describes how the kth-mode is affected by the lth-mode through the overall free-carrier-induced complex-refractive-index perturbation in silicon at (z,t). Finally, $\Delta\beta_{klmn} = -\beta_0^{(k)} + \beta_0^{(l)} - \beta_0^{(m)} + \beta_0^{(n)}$ is a phase-matching term, where $\beta_0^{(k)} = k_0 n_{\mathrm{eff}}^{(k)}$ are the phase-constants at the central frequency ω_0. The expressions for γ_{klmn} and δ_{kl} are

$$\gamma_{klmn} = \frac{3\omega_0\varepsilon_0}{4}\sum_{\mu\alpha\beta\gamma}^{xyz}\iint_{\infty}\chi_{\mu\alpha\beta\gamma}^{(3)}\frac{e_\mu^{*(k)}e_\alpha^{(l)}e_\beta^{*(m)}e_\gamma^{(n)}}{(\mathcal{N}_k\mathcal{N}_l\mathcal{N}_m\mathcal{N}_n)^{1/2}}\mathrm{d}x\mathrm{d}y, \quad (22)$$

$$\delta_{kl}(z,t) = \frac{\omega_0\varepsilon_0 n_{\mathrm{Si}}}{(\mathcal{N}_k\mathcal{N}_l)^{1/2}}\iint_{\infty}\Delta u_{\mathrm{fc}}[\mathbf{e}^{*(k)}\cdot\mathbf{e}^{(l)}]\mathrm{d}x\mathrm{d}y, \quad (23)$$

where, for the kth-mode, $\mathbf{e}^{(k)}$ is the complex-valued vectorial cross-section distribution and $\mathcal{N}_k$ is the normalization integral defined in Section II C. Additionally, $\Delta u_{\mathrm{fc}}(x,y,z,t) = [\Delta n_{\mathrm{fc}} + (i/2k_0)\Delta\alpha_{\mathrm{fc}}] = \sigma_u N$ is the isotropic $\chi^{(1)}$-perturbation [4, 9] due to the free-carriers, where σ_u is the complex-constant introduced in Section II D and $N(x,y,z,t)$ is the cross-sectional distribution of the free-carrier density at (z,t), generated by the combined TPA-effect of all modes in the waveguide.

Equations (19)-(23) describe the coupled-mode propagation under very general conditions. However, these expressions can be significantly simplified in certain situations as pointed out in [13]. Firstly, when the waveguide is symmetric across the x- and/or y-axes, then, it supports a symmetric-set of modes; consequently, using the permutation symmetry of $\chi^{(3)}$ and mode-orthogonality, it can be shown that most of the γ_{klmn} in Eq. (20) are either vanishing or degenerated, thus leading to a considerably smaller set of nonlinear-parameters. Secondly, the spatial-symmetry of Δu_{fc} in waveguides supporting a symmetric set of modes, prescribes that δ_{kk} is the dominant term in T_{fc}^k, since the mode-projection $[\mathbf{e}^{*(k)}\cdot\mathbf{e}^{(l)}]$ eventually restricts the integral in Eq. (23). Thirdly, when the waveguide is strongly birefringent, then many of the non-phase-matched terms in $T_{3\mathrm{o}}^k$ oscillate-rapidly and the system is dominated by the phase-matched terms, unless special treatment is taken. Even though these three corollaries strictly apply to a limited number of practical applications, nevertheless, they approximately apply also for more relaxed conditions. For instance, even when there is a relatively-small waveguide asymmetry, e.g. a different dielectric cladding and substrate material for an SOI-wire (i.e. a y-axis asymmetry), then many of the γ_{klmn} have negligible values, thus leading to a reduced nonlinear-parameter set; that is also the case when the number of supported modes and/or polarizations involved is limited and symmetric (e.g. two TE/TM mode-pairs). The HSP waveguides marginally satisfy these relaxed conditions, and therefore an extended set of γ_{klmn} terms should normally be accounted for.

Focusing on the multimode-extension for the FCE, the dominant δ_{kk}-term in T_{fc}^k can be calculated by plugging Eqs. (10) and (14) into Eq. (23), yielding

$$\delta_{kk}(z,t) = \frac{k_0 n_{\mathrm{Si}}\Gamma_{(k)}}{n_{\mathrm{eff}}^{(k)}}\sigma_u\langle N\rangle_k, \quad (24)$$

where $\langle N\rangle_k$ denotes the cross-sectional overlap of the overall free-carrier density distribution N at (z,t) with the intensity-profile of the kth-mode, $|\mathbf{e}^{(k)}|^2$. The free-carrier generation rate is assumed proportional to the overall power-density rate-of-change dissipated through TPA, as introduced in Section II D. To this end, we need the overall power-density P_T (in W/m^2), which is given by the sum of the power-density carried by each mode, $P_T = \sum_m P_z^{(m)} = \sum_m \tilde{P}_z^{(m)}|A_m|^2$; in this expression, we have used the normalized power-density distribution $\tilde{P}_z^{(m)}$ of the mth-mode, multiplied by its envelope power $|A_m|^2$. Similarly to Eq. (9), the free-carrier generation-rate G is given by

$$G(x,y,z,t) = \frac{\beta_{\mathrm{TPA}}}{2\hbar\omega_0}\left(\sum_{m=1}^{K}\tilde{P}_z^{(m)}|A_m|^2\right)^2. \quad (25)$$

In the CW-regime all time-dependencies disappear, and the effective free-carrier density perturbing the kth-mode at z is given by

$$\langle N\rangle_k = \tau_{\mathrm{fc}}\ \langle G\rangle_k = \frac{\tau_{\mathrm{fc}}}{2\hbar\omega_0}\sum_{m,n=1}^{K}|A_m|^2\ |A_n|^2\ \Xi_{mn}^{(k)}, \quad (26)$$

where the $\Xi_{mn}^{(k)}$ is the multimode generalization of the carrier-field overlap parameter of Eq. (12)

$$\Xi_{mn}^{(k)} = \langle \beta_{\rm TPA} \tilde{P}_z^{(m)} \tilde{P}_z^{(n)} \rangle_k \tag{27}$$

and shows how efficient are the free-carriers generated by the combination of the mth- and nth-modes in perturbating the kth-mode. Equation (26) depicts that, even though the free-carrier density is generated by the combination of all waveguide modes, it eventually affects each one in a different manner. Finally, in the pulsed-regime, each $\langle N \rangle_k$ obeys its proper rate-equation [Eq. (7)] depending on $\langle G \rangle_k$ and $\tau_{\rm fc}$; evidently, this formulation allows for different $\tau_{\rm fc}^{(k)}$ to be used, attributed to each mode.

VI. NONLINEAR DIRECTIONAL COUPLER

In this Section, we present the nonlinear direction coupler (NLDC), a practical integrated component based on HSP waveguides that can be designed and analyzed with the tools presented.

A. Linear and Nonlinear Analysis

The device consists of a coupler formed by two HSP waveguides in proximity, Fig. 8. The coupler, viewed as a single waveguide, supports a pair of supermodes, namely a symmetric and an anti-symmetric one, as for example in Fig. 8(a) and (b), respectively. Feeding an asymmetric input to the coupler results in an excitation of both its supermodes; specifically, launching light into one of the coupler-waveguides results in an approximately equal excitation of the two supermodes. In this situation, the interference (beating) of the supermodes will result in a periodical coupling of the light between the two waveguides. The coupling-length quantifying this beating-period is given by $L_c = \frac{1}{2}\lambda/\Delta n_{\rm eff}^{(S-A)}$, where "$S$" and "$A$" denote the symmetric and antisymmetric mode, respectively. Furthermore, when the two waveguides of the coupler are identical, then the device is synchronized meaning that maximum power-exchange between the waveguides is allowed. Now, if the constituent waveguides additionally support two polarizations, i.e., both TM- and TE-like modes, then the coupler will support two pairs of supermodes. As the coupling-lengths of the two polarizations are generally different, one can tune the coupler cross-section parameters so that $L_c^{\rm TM} = 2L_c^{\rm TE}$. Additionally setting the coupler-length $L = L_c^{\rm TM}$ renders this 2×2 component into a polarization-splitter, where the TE (and TM) modes experience the BAR (and CROSS) state.

Moving on to describe the nonlinear aspects of this component, we point out that as the power of an asymmetric input-excitation increases, then the Kerr-effect increases the refractive-index only inside the input-waveguide, thus desynchronizing the coupler. When this self-focusing induced desynchronization is large enough, $\Delta\beta_{\rm Kerr} L_c > \pi\sqrt{3}$ [16], then, light cannot couple to the opposite waveguide and the output of the L_c-long 2×2 component switches from the CROSS- to the BAR-state. Assuming that the coupler-desynchronization can be associated with the nonlinear phase-shift in a single-waveguide, $\Delta\beta_{\rm Kerr} L_c \approx \Delta\Phi_{\rm NL} = \gamma P_{\rm in} L_{\rm eff}$, the critical input-power for NLDC-switching is estimated by

$$P_{\rm sw} > \frac{\pi\sqrt{3}}{\mathcal{F}[1-\exp(-L_c/L_{\rm prop})]}. \tag{28}$$

This formula prescribes that as the available interaction-length increases ($L_c \gg L_{\rm prop}$) then $P_{\rm sw}$ decreases, at the obvious expense of increased IL. The floor-value is $\pi\sqrt{3}/\mathcal{F}$ while, for a lossless-waveguide ($L_{\rm eff} \equiv L_c$), this expression reduces to $\pi\sqrt{3}/(\gamma L_c)$. Finally, when TPA and FCE come into play in silicon-comprising waveguides, the $P_{\rm sw}$ is expected to increase due to the reduction of the FoM ($\mathcal{F}' < \mathcal{F}$).

The component performance is quantified by the power-crosstalk (XT) between the output-waveguides (ports) at a given polarization, as well as by the insertion-losses. Our multimode NLSE-system corresponds to the slowly-varying field-envelopes of the coupler supermodes (A_S, A_A), however, the inputs and outputs are measured in terms of the left- and right-waveguide phase-corrected field-envelopes (A_L, A_R). Consequently, we initially calculate the $A_{S/A} = (A_L \pm A_R)/\sqrt{2}$ at the coupler-input, we then numerically integrate the system in terms of $A_{S/A}$, and we finally reconstruct the $A_{L/R} = [A_S \exp(i\beta_0^{(S)} z) \pm A_A \exp(i\beta_0^{(A)} z)]/\sqrt{2}$ at the coupler-output (z). That said, the output-waveguide crosstalk for a given polarization is given by ${\rm XT} = |A_L|^2/|A_R|^2$, and the same formulas apply for each polarization.

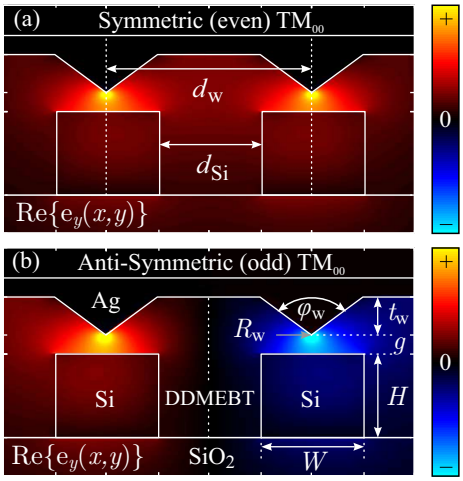

FIG. 8. Electric-field distributions, $\mathrm{Re}\{e_y(x,y)\}$, of the (a) symmetric/even and (b) anti-symmetric/odd TM-like supermodes of a directional-coupler formed by a pair of HSP-waveguides.

B. Design and Performance Evaluation

As described in the previous Section, the NLDC made of HSP waveguides can operate as a power-dependent router for the TM polarization, while being power-insensitive for the TE polarization. In order to design the component, we initially investigate the effect of the lateral spacing [$d_{\rm w}$ in Fig. 8(a)] between the two HSP waveguides on the coupling-lengths of the the TM and TE modes. The rest of the coupler parameters, Fig. 8(b), are set to $W \times H = 320 \times 220$ nm^2, $g = 20$ nm, $t_{\rm w} = 100$ nm, $\varphi_{\rm w} = 53.2^\circ$ and $R_{\rm w} = 1$ nm; the width of the Si-wires was increased to additionally accommodate a well-confined SOI-like TE-mode along with the TM-mode of the HSP waveguide. It can be inferred that the $L_c^{\rm TM}$ depends mainly on $d_{\rm w}$, while the $L_c^{\rm TE}$ additionally depends on W (wider Si-ribs lead to more confined TE modes, increasing $L_c^{\rm TE}$ for the same $d_{\rm w}$). For the selected parameters, it was observed that $L_c^{\rm TM}/L_c^{\rm TE} \approx 2$ for a wide range of spacings $d_{\rm Si} = d_{\rm w} - W = [250, 500]$ nm. Consequently, we focused on three spacings $d_{\rm w} = 600,\ 700,\ 800$ nm that lead to $L_c^{\rm TM} = 14.6, 28.2, 54.0$ μm and $L_c^{\rm TE} = 8.0, 14.9, 27.9$ μm, respectively. In this way, the condition $L_c^{\rm TM}/L_c^{\rm TE} = 2$ is relaxed for the rest of this Section; nevertheless, it can be satisfied with fine-tuning of W for any given $d_{\rm w}$.

Moving on to the nonlinear analysis, we calculate the parameter-set of the four-NLSE equation-system of Eq. (19) for each value of $d_{\rm w}$, adopting a carrier-lifetime of $\tau_{\rm fc} = 0.1$ ns for all FCE-related parameters. Subsequently, we numerically integrate the equations up to $L = L_c^{\rm TM}$ for various CW input-powers. Figure 9(a) depicts the XT for the TE and TM polarizations at the three lateral spacings previously defined, as a function of $P_{\rm in}$ (CW input-power), distributed equally among the supermodes: $A_S(0) = A_A(0) = (\frac{1}{2}P_{\rm in})^{1/2}$. Concerning the TM-polarization, when the $L_c^{\rm TM}$ increases (as the $d_{\rm w}$ increases) then the input-power for the XT-peak is decreased. Specifically, for $d_{\rm w} = 600,\ 700,\ 800$ nm, the respective input-powers were found 18.5, 16, 14 dBW, while the critical NLDC switching-powers from Eq. (28) are $P_{\rm sw} = 16, 14, 12.7$ dBW, respectively ($\mathcal{F} \approx 0.35$ W^{-1} and $L_{\rm prop} \approx 30$ μm for this HSP waveguide); the agreement is satisfactory while the slightly increased powers are due to FCE-degradation. Needless to say that with increasing $L_c^{\rm TM}$, the component IL are increased; however, an additional drawback observed is the reduction of the first XT peak-value, e.g. XT = 13.5, 11, 7 dB at the above input-powers, respectively. This peak-XT reduction is due to the increased dephasing associated with non-phase-matched XPM terms in Eq. (20).

Concerning the TE-polarization, dotted lines in Fig. 9(a), XT > 10 dB in all three cases, as $L = 2L_c^{\rm TE}$ is approximately satisfied for the nominal $W = 320$ nm. The dotted curves are truncated above the CW-power where the average carrier-density, Eq. (11), exceeds 10^{26} m^{-3}. Additionally, the FCD is responsible for a considerable XT-improvement, at certain $P_{\rm in}$ between 12-15 dBW. This is explained by noting that $L_c^{\rm TM}/L_c^{\rm TE} < 2$ for all three $d_{\rm w}$ and that FCD reduces the $n_{\rm eff}$ of TE-modes. Consequently, the $L_c^{\rm TE}$ is decreased and eventually the phase-matching condition is compensated. Moreover, the $d_{\rm w} = 800$ nm (600 nm) coupler is the one closest to (farthest from) satisfying the condition, so a smaller (higher) power is required. In any case, the critical power for NLDC-switching at the TE-polarization is quite high, in the order of $P_{\rm sw} = \pi\sqrt{3}/(\gamma_{\rm TE}L) > 20$ dBW, so this polarization always experiences the BAR-state. Finally, it was noted that cross-polarization coupling was in all cases negligible, e.g. < -40 dB.

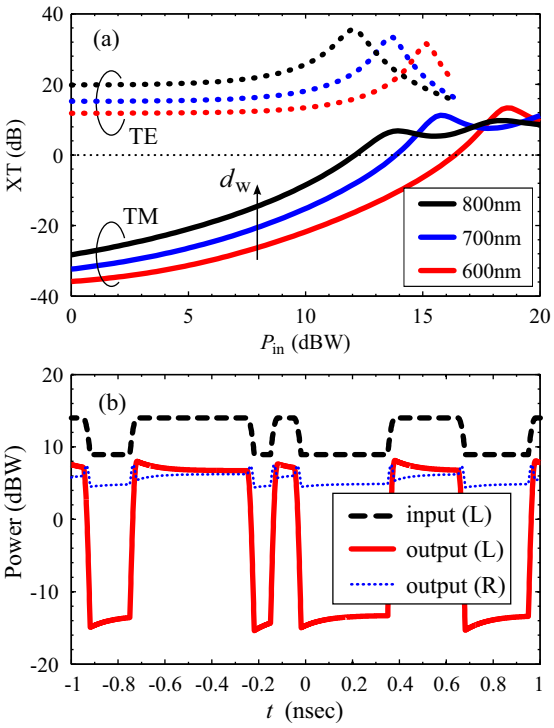

FIG. 9. (a) CW-characterization of the NLDC, i.e., crosstalk between the output-waveguides as a function of the total input-power, for both TM (solid lines) and TE (dotted lines) polarizations. The three HSP-waveguide spacings, $d_{\rm w} = 600,\ 700,\ 800$ nm, correspond to lengths $L = L_c^{\rm TM} = 14.6,\ 28.2,\ 54.0$ μm, respectively. (b) Extinction-ratio increase at the output of the left-waveguide of the NLDC when a TM-polarized 10 GHz NRZ-modulated signal of ER = 5 dB is launched in its left input-waveguide. The peak-power is 14 dBW and the NLDC is 28.2 μm-long ($d_{\rm w} = 700$ nm).

Interestingly, the NLDC additionally offers the possibility of boosting the extinction-ratio (ER) of modulated TM-polarized signals. For instance, examining Fig. 9(a), we observe that an input-power-change of 10 dB (from a $P_{\rm in}$ corresponding to an XT-peak) corresponds to an output-XT-change > 30 dB for the TM-power. Exploiting this feature, we feed a modulated signal to the input of the left coupler-waveguide and calculate the temporal field-envelopes at the output of the coupler-waveguides (left and right). The input temporal-envelope is a 10 Gbps NRZ signal with a 30 psec rise/fall-time, a

14 dBW peak-power (TM) and a poor ER = 5 dB; the coupler is based on the NLDC design with $d_{\rm w} = 700$ nm and $L = L_c^{\rm TM} = 28.2$ μm, previously analyzed. The SSFM was used to numerically integrate the pair of TM-supermode NLSE equations, and dispersion was found to have a negligible impact in these length-scales. In Fig. 9(b), we note that the ER at the output of the left-waveguide (solid red curve) is improved by 15 dB with respect to the input (dashed black curve), with approximately 4.5 dB insertion-losses. The overshoots during the bit-changes in the output-envelope of the right-waveguide (dotted blue curve) correspond to the power-levels where the XT changes its sign [Fig. 9(a)] and, for this NLDC design, they disappear entirely when $P_{\rm in,peak} < 13$ dBW.

VII. CONCLUSIONS

We have rigorously investigated the potential of hybrid silicon-plasmonic (HSP) waveguides for $\chi^{(3)}$-related nonlinear applications in compact integrated photonic components implemented on the prominent silicon-on-insulator platform. We have established a set of figures-of-merit for nonlinear-waveguide characterization that account for nonlinearity, losses, as well as the additional effects arising from the silicon-presence, namely the two-photon-absorption and the resulting free-carrier effects. A nonlinear HSP waveguide design based on the DDMEBT polymer and utilizing an inverted metal-wedge was numerically optimized with respect to these FoM, aiming at a waveguide where the Kerr-effect is not dominated by FCE as the optical power increases. The final design surpasses all similar hybrid plasmonic waveguides in terms of overall performance, while it constitutes a fair alternative to non-plasmonic waveguides. Even though the power-efficiency of these waveguides is still quite low, there are promising indications that it can be further increased with the use of novel nonlinear polymer materials. Finally, the multimode extension of our formulation was used for the modeling of two all-optical applications of a nonlinear directional coupler made of HSP waveguides, namely, a power-dependent polarization-selective switch and an extinction-ratio booster for modulated signals.

ACKNOWLEDGMENTS

This research has been co-financed by the European Union (European Social Fund - ESF) and Greek national funds through the Operational Program "Education and Lifelong Learning" of the National Strategic Reference Framework (NSRF) - Research Funding Program: Heracleitus II. Investing in knowledge society through the European Social Fund. The authors would like to thank Odysseas Tsilipakos for fruitful discussions and insightful remarks.

[1] P. Butcher and D. Cotter, *The Elements of Nonlinear Optics* (Cambridge U. Press, Great Britain, 1990).
[2] G. P. Agrawal, *Nonlinear Fiber Optics* (Academic Press, U.S.A., 2007), 4th ed.
[3] B. Jalali and S. Fathpour, "Silicon photonics," J. Lightwave Technol. **24**, 4600–4615 (2006).
[4] Q. Lin, O. J. Painter, and G. P. Agrawal, "Nonlinear optical phenomena in silicon waveguides: Modeling and applications," Opt. Exress **15**, 16604–16644 (2007).
[5] S. I. Bozhevolnyi, ed., *Plasmonic Nanoguides and Circuits* (Pan Stanford Publishing, Singapore, 2008).
[6] A. V. Krasavin and A. V. Zayats, "Silicon-based plasmonic waveguides," Opt. Exress **18**, 11791–11799 (2010).
[7] M. Wu, Z. Han, and V. Vien, "Conductor-gap-silicon plasmonic waveguides and passive components at subwavelength scale," Opt. Exress **18**, 11728–11736 (2010).
[8] L. Yin and G. P. Agrawal, "Impact of two-photon absorption on self-phase modulation in silicon waveguides," Opt. Lett. **32**, 2031–2033 (2007).
[9] R. A. Soref and B. R. Bennett, "Electrooptical effects in silicon," IEEE J. Quantum Electron. **QE-23**, 123–129 (1987).
[10] R. F. Oulton, V. J. Sorger, D. A. Genov, D. F. P. Pile, and X. Zhang, "A hybrid plasmonic waveguide for subwavelength confinement and long-range propagation," Nat. Photonics **2**, 496–500 (2008).
[11] C. Koos, P. Vorreau, T. Vallaitis, P. Dumon, W. Bogaerts, R. Baets, B. Esembeson, I. Biaggio, T. Michinobu, F. Diederich, W. Freude, and J. Leuthold, "All-optical high-speed signal processing with silicon-organic hybrid slot waveguides," Nat. Photonics **3**, 216–219 (2009).
[12] S. M. Jensen, "The nonlinear coherent coupler," IEEE J. Quantum Electron. **QE-18**, 1580–1583 (1982).
[13] B. A. Daniel and G. P. Agrawal, "Vectorial nonlinear propagation in silicon nanowire waveguides: Polarization effects," J. Opt. Soc. Am. B **27**, 956–965 (2010).
[14] A. Liu, L. Liao, D. Rubin, H. Nguyen, B. Ciftcioglu, Y. Chetrit, N. Izhaky, and M. Paniccia, "High-speed optical modulation based on carrier depletion in a silicon waveguide," Opt. Exress **15**, 660–668 (2007).
[15] S. Afshar Vahid and T. M. Monro, "A full vectorial model for pulse propagation in emerging waveguides with subwavelength structures part i: Kerr nonlinearity," Opt. Exress **17**, 2298–2318 (2009).
[16] A. W. Snyder and J. D. Love, *Optical Waveguide Theory* (Chapman and Hall, U.S.A., 1983).
[17] I. D. Rukhlenko, M. Premaratne, and G. P. Agrawal, "Nonlinear propagation in silicon-based plasmonic waveguides from the standpoint of applications," Opt. Exress **19**, 206–217 (2011).
[18] D. Dimitropoulos, R. Jhaveri, R. Claps, J. C. S. Woo, and B. Jalali, "Lifetime of photogenerated carriers in silicon-

on-insulator rib waveguides," Appl. Phys. Lett. **86**, 1–3 (2005).

[19] D. Dai, Y. Shi, S. He, L. Wosinski, and L. Thylen, "Gain enhancement in a hybrid plasmonic nano-waveguide with a low-index or high-index gain medium," Opt. Exress **19**, 12925–12936 (2011).

[20] Y. Bian, Z. Zheng, Y. Liu, J. Liu, J. Zhu, and T. Zhou, "Hybrid wedge plasmon polariton waveguide with good fabrication-error- tolerance for ultra-deep-subwavelength mode confinement," Opt. Exress **19**, 22417–22422 (2011).

[21] M. M. Hossain, M. D. Turner, and M. Gu, "Ultrahigh nonlinear nanoshell plasmonic waveguide with total energy confinement," Opt. Exress **19**, 23800–23808 (2011).

[22] B. Esembeson, M. L. Scimeca, T. Michinobu, F. Diederich, and I. Biaggio, "A high-optical quality supramolecular assembly for third-order integrated nonlinear optics," Adv. Mater. **20**, 4584–4587 (2008).

[23] B. L. Lawrence, M. Cha, J. U. Kang, W. Toruellas, G. Stegeman, G. Baker, J. Meth, and S. Etemad, "Large purely refractive nonlinear index of single crystal p-toluene sulphonate (pts) at 1600 nm," Electron. Lett. **30**, 447–448 (1994).

[24] F. Qin, Z. Meng, X. Zhong, Y. Liu, and Z. Li, "Fabrication of semiconductor-polymer compound nonlinear photonic crystal slab with highly uniform infiltration based on nanoimprint lithography technique," Opt. Exress **20**, 13091–13099 (2012).

[25] A. Zakery and S. R. Elliott, "Optical properties and applications of chalcogenide glasses: A review," J. Non-Cryst. Solids **330**, 1–12 (2003).

[26] P. Ginzburg, A. Hayat, N. Berkovitch, and M. Orenstein, "Nonlocal ponderomotive nonlinearity in plasmonics," Opt. Lett. **35**, 1551–1553 (2010).

[27] O. Tsilipakos, A. Pitilakis, A. C. Tasolamprou, T. V. Yioultsis, and E. E. Kriezis, "Computational techniques for the analysis and design of dielectric-loaded plasmonic circuitry," Opt. Quantum Electron. **42**, 541–555 (2011).

[28] A. Pitilakis, O. Tsilipakos, and E. E. Kriezis, "Nonlinear effects in hybrid plasmonic waveguides," in "International Conference on Transparent Optical Networks," 6254436, (2012).

[29] A. Boltasseva, V. S. Volkov, R. B. Nielsen, E. Moreno, S. G. Rodrigo, and S. I. Bozhevolnyi, "Triangular metal wedges for subwavelength plasmon-polariton guiding at telecom wavelengths," Opt. Exress **16**, 5252–5260 (2008).

[30] E. Dulkeith, Y. A. Vlasov, X. Chen, N. C. Panoiu, and R. M. Osgood Jr., "Self-phase-modulation in submicron silicon-on-insulator photonic wires," Opt. Exress **14**, 5524–5534 (2006).

[31] C. Milian and D. V. Skryabin, "Nonlinear switching in arrays of semiconductor on metal photonic wires," Appl. Phys. Lett. **98** (2011).